Comparison of Kinetic and Fluid Models for Tungsten Impurity Transport with SOLPS-IMPGYRO

M. Toma[a]*, X. Bonnin[b], Y. Sawada[a], Y. Homma[a], A. Hatayama[a], K. Hoshino[c], D. Coster[d], R. Schneider[e]

[a]Keio University, 3-14-1 Hiyoshi Kouhoku, 223-8522 Yokohama, Japan.
[fb]LSPM - CNRS, Université Paris 13, Sorbonne Paris Cité, 99 Avenue Jean-Baptiste Clément, F-93430 Villetaneuse, France.
[c]Japan Atomic Energy Agency, 2-166 Oaza-Obuchi-aza-Omotedate, 039-3212 Rokkasho, Japan.
[d]Max-Planck-Institut für Plasmaphysik, Boltzmannstr 2, D-85748 Garching, Germany.
[e]Ernst-Moritz-Arndt University Greifswald, Felix-Hausdorff Str. 6, D-17487 Greifswald, Germany.

Abstract

A benchmark calculation comparing kinetic modeling with IMPGYRO and multi-fluid modeling with SOLPS for tungsten impurities has been performed. In both cases, impurity densities are relatively large in the top SOL region mainly due to the effect of the thermal force. In the outer divertor region, however, a significant difference has been observed, which could be explained by the effect of the drifts. The drifts are switched off in SOLPS in this study, while they are naturally taken into account in IMPGYRO. The drifts prevent impurities from being transported toward the outer divertor region.

PACS: 52.25.Vy 52.30.Ex 52.55.Fa 52.65.Pp

PSI-20 keywords: Divertor modeling, Tungsten, Impurity transport, B2/EIRENE, IMPGYRO

**Corresponding author address:* 3-14-1 Hiyoshi, Kouhoku, Yokohama, Japan.

**Corresponding author E-mail:* toma@ppl.appi.keio.ac.jp

Presenting author: Mitsunori Toma

Presenting author e-mail: toma@ppl.appi.keio.ac.jp

1. Introduction

Aiming to make predictions for tokamaks with tungsten walls, it is necessary to develop simulation codes which precisely analyze erosion of tungsten plates, impurity transport in SOL/divertor plasma and W penetration into the core plasma. The high-Z impurity transport code IMPGYRO [1] has been developed for such a purpose.

There are two types of impurity transport models, based on either fluid or kinetic approaches. IMPGYRO is a full-orbit kinetic code and has the following advantages compared with a fluid model: i) the code directly follows test particle trajectories, and therefore ii) $\boldsymbol{E}\times\boldsymbol{B}$ and $\boldsymbol{B}\times\nabla B$ drifts are naturally taken into account under given fields, iii) various collision processes act on impurities such as ionization, recombination and Coulomb collisions with background particles, iv) interactions with wall materials (self-sputtering and reflection) are simulated more directly, i.e., IMPGYRO has been coupled with the EDDY code [2,3], and finally v) the model can be applied for plasmas of any collisionality, while the fluid model is applicable only under high collisionality conditions. In addition, the code has been coupled with the SOLPS code package [4] for self-consistent evolution of impurities with the background fuel plasma [5].

The computational cost for such kinetic calculations, however, is very high in order to obtain results with good statistical accuracy. Even for the fluid modeling, multi-fluid treatment for tungsten ions requires large computational resources because of the many charge states. Recently, it has been shown that an advanced scheme which bundles charge states into fewer super-stages is effective to partially

suppress the computational cost, but at the expense of result accuracy [6].

A comparative study between the kinetic modeling with IMPGYRO and the multi-fluid modeling with SOLPS for tungsten impurities is presented in this article.

2. Calculation setups for comparison

2.1 Geometrical model and basic plasma parameters

Figure 1 shows the numerical grid used for the present comparative study. Thisgrid represents an ASDEX-Upgrade geometry and its MHD equilibrium calculation data (shot #16151, a standard SOLPS benchmark grid). A zoom-in view of the divertor region is also shown in Fig. 1(b).

The toroidal magnetic field value at the geometrical center of plasma is 2.7T and has a counter-clockwise direction when seen from above the torus, i.e., the ion ∇B drift is directed towards the top of the device. The plasma current I_p is 1MA and the poloidal magnetic field had a counter-clockwise direction in a poloidal surface with the axis of the torus on the left hand side. In the present study, we assume that plasma consists of deuterium (D) and tungsten impurities (W) only. In order to conduct the comparative study, the following two cases have been calculated:

Case A: Deuterium and tungsten transport are calculated by multi-fluid modeling with B2.5 in SOLPS.

Case B: Tungsten transport is calculated by Monte-Carlo test particle modeling with IMPGYRO, with fixed deuterium plasma as background.

In the present study, we focus mainly on tungsten transport and the same background plasma is used for case A and case B in the following manner. First, we have done the calculation for case A, and obtained a steady-state solution for both background plasma and tungsten impurities. Next, we have done the IMPGYRO calculation in the trace impurity limit, using the same background plasma profiles as those for case A.

2.2 Transport models

Since IMPGYRO solves neutral particles of tungsten kinetically, a calculation with EIRENE would be preferable for comparison. However, afluid model for the neutrals has been adopted in case A for simplicity. Tungsten impurities ionize up to charge states in the low teens in the SOL with relatively low electron temperature below 100eV. Therefore, B2.5 calculates each charge state as an individual fluid species for the charge states from neutral to +14, and a super-stage combining charges +15 to +74 for computational cost reduction.

Radial transport parameters are uniformly and statically given as $D = 0.4\mathrm{m}^2/\mathrm{s}$, $\chi_\mathrm{e} = \chi_\mathrm{i} = 1.6\mathrm{m}^2/\mathrm{s}$ in case A. In IMPGYRO, the anomalous radial displacement per time step Δt has been modeled as $\Delta r = \zeta\sqrt{2D\Delta t}$, where ζ is a standard normal random number. The coefficient D is set to be $0.4\mathrm{m}^2/\mathrm{s}$ in case B. Anomalous contributions are not imposed on parallel transport; which is considered to be classical in both cases.

In case A, $\boldsymbol{E}\times\boldsymbol{B}$ and $\boldsymbol{B}\times\nabla B$ drifts are switched off. On the other hand, both drifts are naturally taken into account (for W ions) in case B, because IMPGYRO directly solves the equations of motion for impurity ions with their gyro motions. Although the drifts should be switched on also in case A, they are switched off in the present study. Were drifts present in case A, it would become difficult to distinguish the influence of drifts on the tungsten impurities. Indeed, the drifts change the background plasma profiles [7], which in turn affect the impurity transport. Therefore, we have switched off the effects of drifts in

case A as a first step of the comparative study.

2.3 Boundary conditions and impurity sources

Deuteron density $n_{D+} = 2.0 \times 10^{19} / \mathrm{m}^3$ and input powers $Q_e = Q_i = 1.0\mathrm{MW}$ at the core-side boundary are kept throughout the calculation. Tungsten test particles which reach the core-side and the wall-side boundaries are removed from the calculation in case B. To take similar boundary conditions for tungsten species, a leakage option with a factor $\alpha = 1.0$ is applied to those boundaries in case A. At the both inner and outer target plates, physical sputtering and reflection are taken into account, via TRIM data in case A, and via the EDDY code in case B.

Tungsten neutrals are fed at a constant generation rate of $1.0 \times 10^{18} / \mathrm{s}$ from an artificial point source near the outer midplane as shown in Fig. 1 in both cases. The tungsten generation condition is based on a measurement of tungsten influx from an ICRH limiter in ASDEX-Upgrade [8]. The generated tungsten neutrals are assumed to have a velocity $\boldsymbol{v} = 0\mathrm{m/s}$.

3. Results and Discussions

Two dimensional (2D) density profiles of tungsten impurities in the poloidal cross-section are shown in Fig. 2. All the charge states are summed up. First, we focus on the upstream region of the SOL near the top. In both cases A and case B, impurity densities tend to be larger in this region. Along the poloidal direction, the densities peak at the position where the point source of impurities is located. Figure 3 shows the background ion flow velocity along the magnetic field. The stagnation point of the background ion flow is very close to the point source, which is shown in Fig. 1 with the cross, in this calculation. Thus, the impurities start to be transported by other mechanisms than the background ion flow. Figure 4 shows ion and electron temperature profiles along the magnetic field line. The ion and electron temperatures start decreasing roughly around $x \approx -2.1\mathrm{m}$ and $x \approx 0.3\mathrm{m}$ in the inner and outer SOL, respectively. The temperature gradients ∇T_i and ∇T_e start increasing towards the inner and outer target plates from these points. The effect of the thermal force becomes larger and is directed towards the top. As a result, impurities are transported towards the top where the temperature profiles are relatively flat. The impurity densities become larger in the region between the inner and outer midplane. From these results, the thermal force plays a key role to explain the impurity density profile shown in Fig. 2 in both cases.

Next, we focus on the impurity profile in the inner divertor region. In both cases, the impurity densities are very low close to the separatrix, while they become larger radially far from the separatrix. Figure 5 shows the radial profile of the net forces, which is the sum of the friction and the thermal force, acting on the impurities in the vicinity of the X-point on the high field side ($x \approx 3.2\mathrm{m}$). The force is directed

towards upstream near the separatrix, while it is directed towards the target far from the separatrix. The direction is governed by the balance between the friction and the thermal forces. Figure 6 shows the radial profiles of electron temperature and deuterium density along the inner target. The electron temperature near the strike point decreases to $T_e \approx 3\text{eV}$ and the neutral density increases to $n_{D0} \approx 2\times10^{20}/\text{m}^3$. Then, ion parallel momentum and flow velocity towards the target could be reduced near the separatrix due to the momentum loss by ion-neutral collisions. Therefore, the friction force becomes smaller than the thermal force, and the net force is directed towards the upstream near the separatrix in the vicinity of the X-point.

Finally, we discuss the impurity density profile in the outer divertor region. The impurity density profile in case A shows in-out symmetry, and the impurity density profile in the outer divertor region has roughly the same features as that of the inner divertor region. In case B, however, the impurities are hardly transported towards the outer target at all, as shown in Fig. 2. The difference could be explained by the effects of drifts. The drifts have been switched off in case A, while they have been naturally taken into account in case B. The $\boldsymbol{E}\times\boldsymbol{B}$ drift in the SOL and in the private flux regions rotates counter-clockwise in the poloidal surface in this case. The ion $\boldsymbol{B}\times\nabla B$ drift is directed towards the top of the device. The radial profile of electric potential and toroidal magnetic field at the poloidal position $x=0$ is shown in Fig. 7. Using the values of $\boldsymbol{E}$ and $\boldsymbol{B}$ from Fig. 7, the $\boldsymbol{E}\times\boldsymbol{B}$ drift velocity is estimated to be 1000m/s, while the $\boldsymbol{B}\times\nabla B$ drift velocity is less than 10m/s, at the position where the point source is located. The $\boldsymbol{E}\times\boldsymbol{B}$ drift velocity is compared with the background flow velocity in Fig. 8. The $\boldsymbol{E}\times\boldsymbol{B}$ drift velocity

is dominant for the impurity velocity if the impurity flow velocities is completely relaxed with the background flow velocities around the point source. The generated impurity neutrals ionize almost immediately after their birth near the outer midplane, because the electron temperature is relatively high there. The effects of thermal force are relatively small as discussed above in Fig. 4. In case A, the effects of drifts are also switched off. Although the friction force is not as large as in the divertor region close to the target plate, it seems to drive the impurity ions towards the outer target plate in case A. Then, they reach the outer target in case A. With the drifts in case B, however, the impurity ions are mainly transported upstream by the drifts, because the $\boldsymbol{E} \times \boldsymbol{B}$ drift is dominant in case B as shown in Fig. 8. Thus, impurities are mostly transported towards the top from their birth point, and some of them reach the inner target in case B. This makes the inner and the outer density profile more asymmetric than those in case A.

4. Summary

A benchmark comparative calculation for tungsten-impurity transport between kinetic modeling by IMPGYRO and fluid modeling by SOLPS has been performed. The impurity densities tend to be larger in the upstream region of the SOL due to the thermal force in both cases.

On the high field side, especially in the inner divertor region, the impurities can hardly approach the target through flux tubes near the separatrix. The friction force near the X-point is relatively small due to the partially detached plasma, and then the thermal force is larger than the friction force. As a result, the net force is directed upstream and impurity ions are transported upstream.

In the outer divertor region, a significant difference on the impurity densities is observed. The difference could be explained by drifts; the drifts are switched off in SOLPS in this study and they are naturally taken into account in IMPGYRO. The drifts transport the impurities towards the upstream of the SOL; therefore, they prevent impurities to be carried toward the outer divertor region. A comparison with a SOLPS calculation including the effects of the drifts should be performed in the near future.

References

[1] I. Hyodo et al., J. Nucl. Mater. 313-316 (2003) 1183.

[2] K. Ohya, Physica Scr. T124 (2006) 70.

[3] M. Toma et al., J. Nucl. Mater. 390-391, (2009) 207.

[4] R. Schneider et al., Contrib. Plasma Phys. 46 (2006) 3.

[5] M. Toma et al., Contrib. Plasma Phys. 52 (2012) 450.

[6] X. Bonnin et al., J. Nucl. Mater. 415 (2011) S488.

[7] V. Rozhansky et al., J. Nucl. Mater. 313-316 (2003) 1141.

[8] R. Dux et al., J. Nucl. Mater. 363-365 (2007) 112.

Figure captions

Figure 1

(a) Numerical mesh for whole computational domain. The point source location is shown by a cross. The local coordinate system (x: poloidal, y: radial) is also shown. (b) A zoom-in view of the divertor region.

Figure 2

2D density profiles of tungsten impurity in poloidal cross-section. The densities for all the charge states are summed up and the results are plotted: (a) by B2.5 fluid code (case A) and (b) by IMPGYRO kinetic code (case B).

Figure 3

Flow velocity of the background ions along the field line.

Figure 4

Ion and electron temperatures along the field line.

Figure 5

Radial profile of the net forces acting on the impurities at the entrance to the inner divertor region. Negative value means toward the inner target. Note that the right hand side corresponds to the separatrix

($y = 0$).

Figure 6

Electron temperature and D neutral density along the inner target plate. Note that the right hand side corresponds to the separatrix ($y = 0$) as in Fig. 5.

Figure 7

Radial profile of electric potential and toroidal magnetic field at the point source ($x = 0$).

Figure 8

Ratio of $\boldsymbol{E} \times \boldsymbol{B}$ drift velocity divided by D flow velocity along the field line which passes through the point source.

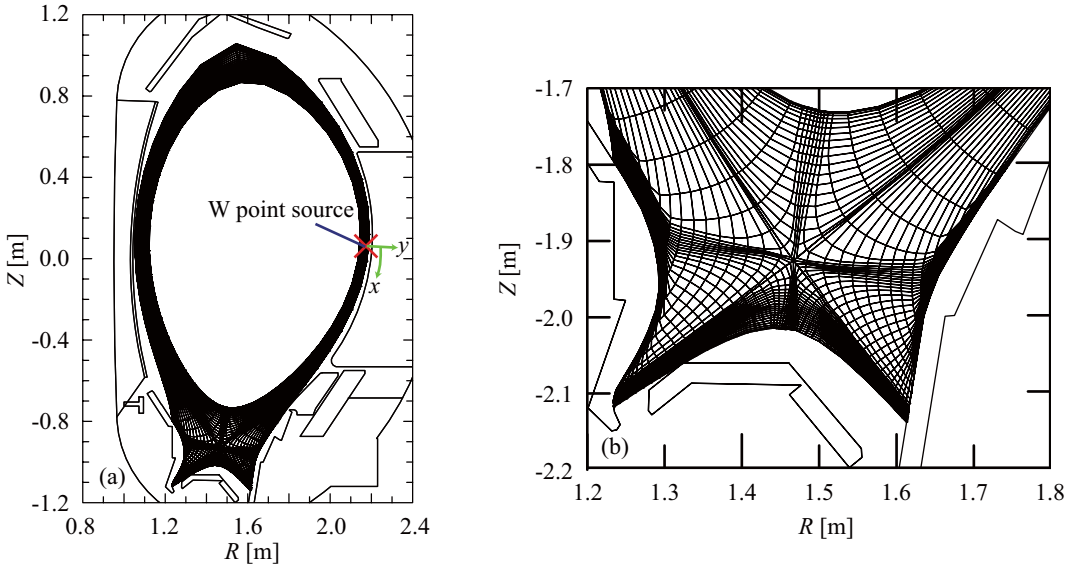

Figure 1 (160mm wide)

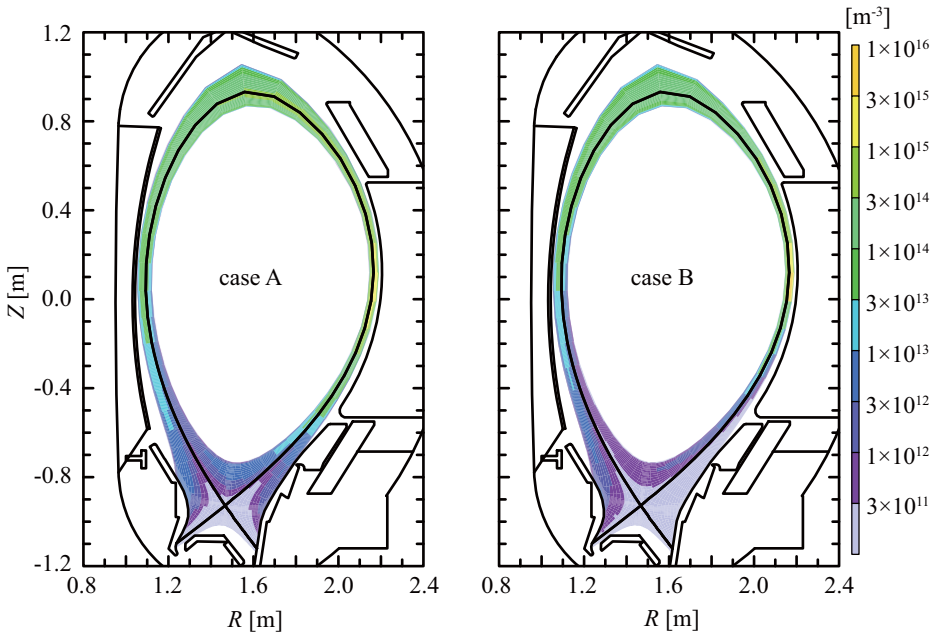

Figure 2 (160mm wide)

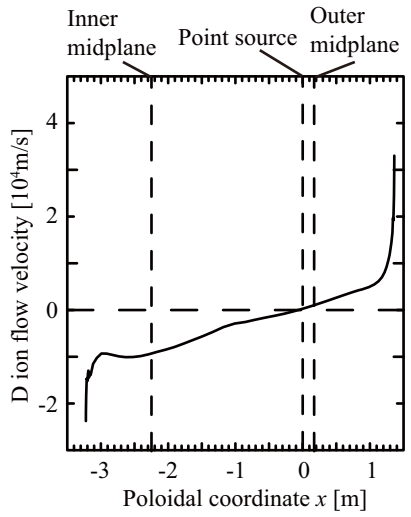

Figure 3 (75mm wide)

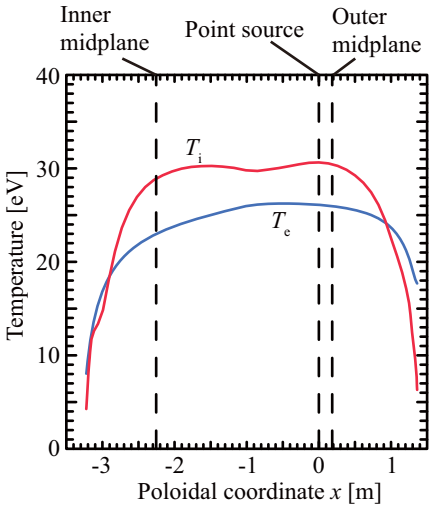

Figure 4 (75mm wide)

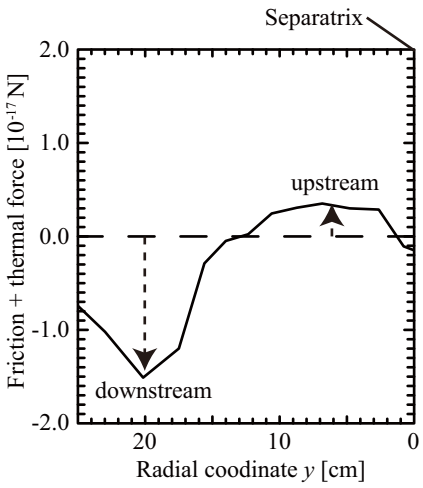

Figure 5 (75mm wide)

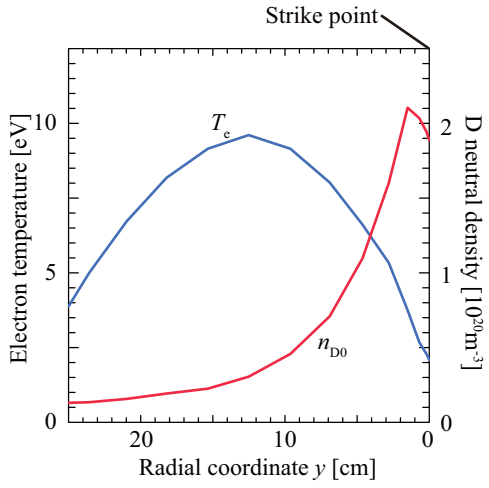

Figure 6 (75mm wide)

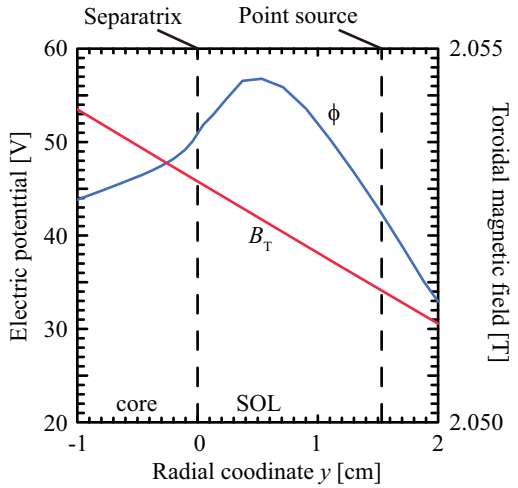

Figure 7 (75mm wide)

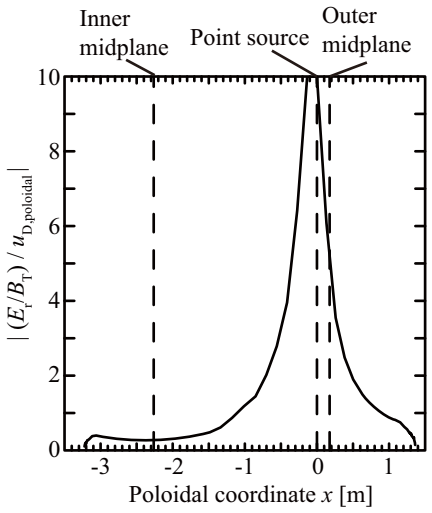

Figure 8 (75mm wide)